Hindawi
Advances in Mathematical Physics
Volume 2020, Article ID 4890152, 16 pages
https://doi.org/10.1155/2020/4890152

Research Article

Double Stratified Mixed Convective Flow of Couple Stress Nanofluid past Inclined Stretching Cylinder Using Cattaneo-Christov Heat and Mass Flux Model

Wubshet Ibrahim [1] and Gosa Gadisa [2]

[1] *Department of Mathematics, Ambo University, Ambo, Ethiopia*
[2] *Department of Mathematics, Wollega University, Nekemte, Ethiopia*

Correspondence should be addressed to Wubshet Ibrahim; wubshetib@yahoo.com

Received 22 December 2019; Accepted 9 April 2020; Published 8 May 2020

Academic Editor: Remi Léandre

In this exploration, a double stratified mixed convective flow of couple stress nanofluid past an inclined stretching cylinder using a Cattaneo-Christov heat and mass flux model is considered. The governing partial differential equation of the boundary layer flow region is reduced to its corresponding ordinary differential equation using a similarity transformation technique. Then, the numerical method called the Galerkin finite element method (GFEM) is applied to solve the proposed fluid model. We performed a grid-invariance test or grid-convergence test to confirm the convergence of the series solution. The effects of the different noteworthy variables on velocity, temperature, concentration, local skin friction, local Nusselt number, and local Sherwood number are analyzed in both graphical and tabular forms. We have compared our result with the existing results in the literature, and it is shown that GFEM is accurate and efficient. Moreover, our result shows that the velocity field is retarded when the angle of inclination enhances and the heat transfer rate is reduced with larger values of the curvature of the cylinder.

1. Introduction

Most recently, the investigation of fluid flow around a stretching cylinder has gained much consideration by different scholars. This is due to the fact that many industrial applications like geothermal power generation, spinning of fiber, drilling operations, and plastic sheet extrusion may grip the boundary layer flow around the stretching cylinder. In the above point of view, Majeed et al. [1] introduced heat transfer due to the stretching cylinder and solved it using the Chebyshev spectral Newton iterative scheme. The boundary layer flow of a nanofluid past a permeable stretching cylinder is analyzed by Hayat et al. [2]. They inspected that curvature and suction/injection effects on a local skin friction coefficient are similar. Hayat et al. [3] explained the mathematical model for a mixed convection flow past an inclined cylinder and solved it numerically by the homotopy analysis method.

Stratified effects are prominent in the study of fluid dynamics and industrial engineering, for instance, heat rejection process to the environments (rivers, oceans, and lakes) and thermal energy storage systems such as solar ponds. Stratification of the fluid is a deposition or formation of layers that arise because of temperature difference, concentration difference, or existence of different fluids [4]. The thermal/solutant stratifications of hydrogen and oxygen in lakes may affect the growth rates of all cultured species. This initiated different researchers to divert their attention to investigate the effects of stratifications in the area of fluid dynamics. A dual stratification effect on a mixed convection flow of the non-Newtonian fluid (Eyring-Powell) past an inclined cylinder with heat generation/absorption is reported by Rehman et al. [5]. They employed a shooting technique with the fifth-order Runge-Kutta scheme to solve the coupled differential equations. Authors [6–10] analyzed the effects of a double stratified flow over a stretching cylinder with the

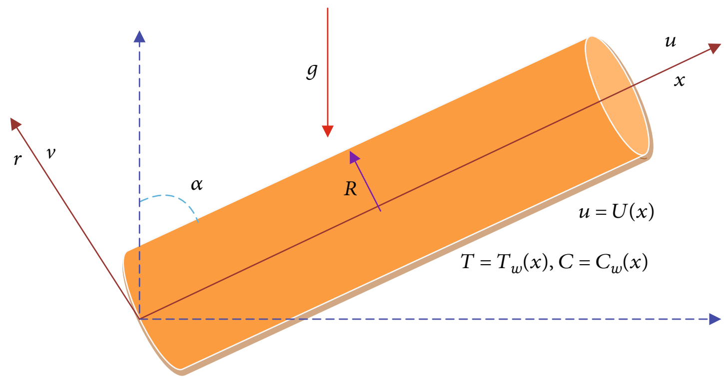

Figure 1: Flow diagram.

impacts of different governing parameters. They used the Fourier law of heat conduction to analyze the heat transfer rate in the boundary layer flow region. Very recently, researchers like Ijaz and Ayub [11] have investigated the Jeffery fluid flow with effects of thermal stratification, homogeneous-heterogeneous, and new heat flux model past a stretching cylinder.

Moreover, various scholars have investigated the non-Newtonian fluid flow around a cylinder with the impacts of the non-Fourier law model. Raju et al. [12] analyzed the MHD flow past a stretching cylinder with the Cattaneo-Christov heat flux model. In their study, the coupled differential equations were solved numerically by employing RK4 along shooting technique. Ibrahim and Hindebu [13] applied the Keller-box method to solve the MHD boundary layer flow of the non-Newtonian fluid around a stretching cylinder with the Cattaneo-Christov heat and mass model. Gangadhar et al. [14] also elaborated a slip flow past a cylinder using the effects of the Cattaneo-Christov model. Later on, Kumar et al. [15] reported a Williamson and Casson fluid flow past a stretching cylinder with the Cattaneo-Christov model.

From the above brief investigation, it has been noticed that the problem of the double stratified mixed convection couple stress nanofluid flow past an inclined cylinder with the Cattaneo-Christov heat and mass flux model has not been yet considered. Asad et al. [16] studied the flow of a couple stress fluid in the presence of variable thermal conductivity. In the present study, additional effects such as mixed convection, nanofluid, double stratified, and the Cattaneo-Christov heat and mass flux model are taken into consideration. We employed the influential numerical method for solving engineering and fluid dynamics problems called the Galerkin finite element method carried out in equations (20)–(29) to solve coupled nonlinear differential equations governing the boundary layer flow.

2. Mathematical Modeling

We aspire to analyze the double stratified mixed convective flow of a couple stress nanofluid past an inclined stretching cylinder using the Cattaneo-Christov heat flux model. The flow is produced because of an inclined cylinder. It is assumed that the flow is two-dimensional, steady, and laminar, has a nonslip boundary, and is incompressible. The angle between the stretching cylinder and the vertical axis (x-axis) is α. The flow velocity components x and r are assumed perpendicular to each other as shown in Figure 1. Based on these assumptions and the boundary layer approximation theory, the governing equations are written as follows:

$$\frac{\partial(ru)}{\partial x} + \frac{\partial(rv)}{\partial x} = 0, \tag{1}$$

$$\begin{aligned} u\frac{\partial u}{\partial x} + v\frac{\partial u}{\partial r} &= \nu\left(\frac{\partial^2 u}{\partial r^2} + \frac{1}{r}\frac{\partial u}{\partial r}\right) - \nu'\left(\frac{\partial^4 u}{\partial r^4} + \frac{2}{r}\frac{\partial^3 u}{\partial r^3} \right.\\ &\quad \left. - \frac{1}{r^2}\frac{\partial^2 u}{\partial r^2} + \frac{1}{r^3}\frac{\partial u}{\partial r}\right) + (\Lambda_1(T - T_\infty) \\ &\quad + \Lambda_2(C - C_\infty)^2 + \Lambda_3(T - T_\infty) \\ &\quad + \Lambda_4(C - C_\infty)^2)g\cos\alpha, \end{aligned} \tag{2}$$

$$\begin{aligned} u\frac{\partial T}{\partial x} + v\frac{\partial T}{\partial r} &+ \lambda_E\left\{u^2\frac{\partial^2 T}{\partial x^2} + v^2\frac{\partial^2 T}{\partial r^2} + 2uv\frac{\partial^2 T}{\partial x \partial r} + u\frac{\partial u}{\partial x}\frac{\partial T}{\partial x}\right. \\ &\left. + u\frac{\partial v}{\partial x}\frac{\partial T}{\partial r} + v\frac{\partial u}{\partial r}\frac{\partial T}{\partial x} + v\frac{\partial v}{\partial r}\frac{\partial T}{\partial r}\right\} = \alpha_f\left(\frac{\partial^2 T}{\partial r^2} + \frac{1}{r}\frac{\partial T}{\partial r}\right) \\ &+ \tau\left(D_B\frac{\partial C}{\partial r}\frac{\partial T}{\partial r} + \frac{D_T}{T_\infty}\left(\frac{\partial T}{\partial r}\right)^2\right), \end{aligned} \tag{3}$$

$$\begin{aligned} u\frac{\partial C}{\partial x} + v\frac{\partial C}{\partial r} &+ \lambda_C\left\{u^2\frac{\partial^2 C}{\partial x^2} + v^2\frac{\partial^2 C}{\partial r^2} + 2uv\frac{\partial^2 C}{\partial x \partial r} + u\frac{\partial u}{\partial x}\frac{\partial C}{\partial x}\right. \\ &\left. + u\frac{\partial v}{\partial x}\frac{\partial C}{\partial r} + v\frac{\partial u}{\partial r}\frac{\partial C}{\partial x} + v\frac{\partial v}{\partial r}\frac{\partial C}{\partial r}\right\} = D_B\left(\frac{\partial^2 C}{\partial r^2} + \frac{1}{r}\frac{\partial C}{\partial r}\right) \\ &+ \frac{D_T}{T_\infty}\left(\frac{\partial^2 T}{\partial r^2} + \frac{1}{r}\frac{\partial T}{\partial r}\right). \end{aligned} \tag{4}$$

The related boundary conditions are given as follows:

$$\begin{aligned} u(x,r) &= U(x) = \frac{U_0}{L}x, v(x,r) = 0 \text{ at } r \\ &= R \text{ and } u(x,r) \longrightarrow 0 \text{ as } r \longrightarrow \infty, \\ T(x,r) &= T_w(x) = T_0 + \frac{bx}{L}, C(x,r) \\ &= C_w(x) = C_0 + \frac{dx}{L} \text{ at } r = R, \\ T(x,r) \longrightarrow T_\infty(x) &= T_0 + \frac{cx}{L}, C(x,r) \longrightarrow C_\infty(x) \\ &= C_0 + \frac{ex}{L} \text{ as } r \longrightarrow \infty, \end{aligned} \tag{5}$$

where g, β_C, β_T, and α are gravity, coefficient of concentration expansion, coefficient of thermal expansion, and inclination of the cylinder with x-axis, respectively. Moreover, $T_W(x)$ denotes the prescribed surface temperature, $C_W(x)$ denotes the prescribed surface concentration, $T_\infty(x)$ denotes the variable ambient temperature, $C_\infty(x)$denotes the variable ambient concentration, T_0 denotes the reference temperature, C_0 denotes the reference concentration, U_0 denotes the free stream velocity, and L denotes the reference length.

The stream function ψ which identically satisfies the continuity equation (1) can be defined as

$$u = \frac{1}{r}\left(\frac{\partial \psi}{\partial r}\right), v = -\frac{1}{r}\left(\frac{\partial \psi}{\partial r}\right). \tag{6}$$

The nonlinear partial differential equations (1)–(4) with the associated boundary condition in equation (6) can be reduced to the equivalent nonlinear ordinary differential equations using the following similarity transformations:

$$\begin{aligned} u &= \frac{U_o}{L}xf'(\eta), v = -\frac{R}{r}\sqrt{\frac{U_0\nu}{L}}f(\eta), \eta = \frac{r^2 - R^2}{2R}\left(\frac{U_0}{\nu L}\right)^{1/2}, \psi \\ &= \left(\frac{U_0 \nu x^2}{L}\right)^{1/2} Rf(\eta), \theta(\eta) = \frac{T - T_\infty}{T_w - T_0}, \varphi(\eta) = \frac{C - C_\infty}{C_w - C_0}. \end{aligned} \tag{7}$$

Equations (6) and (7) are combined to produce the following associated ordinary differential equations governing the boundary layer flow:

$$\begin{aligned} &(1 + 2\gamma\eta)f^{(3)} + 2\gamma f^{(2)} - f'^2 + ff^{(2)} \\ &\quad - K \operatorname{Re}\left(8\gamma^2 f^{(3)} + 8(1 + 2\gamma\eta)\gamma f^{(4)} + (1 + 2\gamma\eta)^2 f^{(5)}\right) \\ &\quad + \lambda_m \theta(1 + \beta_t \theta) \cos\alpha + \lambda_m N \varphi(1 + \beta_c \varphi) \cos\alpha = 0, \end{aligned} \tag{8}$$

$$\begin{aligned} &(1 + 2\gamma\eta)\theta'' + 2\gamma\theta' + \Pr \text{Nb}(1 + 2\gamma\eta)\theta'\varphi' \\ &\quad + \Pr \text{Nt}(1 + 2\gamma\eta)\theta'^2 - \Pr\left((\theta + \delta_1)f' - f\theta'\right) \\ &\quad - \Pr \gamma_E\left[f^2\theta'' - ff'\theta' + f'^2(\theta + \delta_1) - (\theta + \delta_1)ff''\right] = 0, \end{aligned} \tag{9}$$

$$\begin{aligned} &(1 + 2\gamma\eta)\left(\varphi'' + \frac{\text{Nt}}{\text{Nb}}\theta''\right) + 2\gamma\left(\varphi' + \frac{\text{Nt}}{\text{Nb}}\theta'\right) \\ &\quad - \text{Sc}\left((\varphi + \delta_2)f' - f\varphi'\right) - \text{Sc}\gamma_C\left[f^2\varphi'' - ff'\varphi'\right. \\ &\quad \left. + f'^2(\varphi + \delta_2) - (\varphi + \delta_2)ff''\right] = 0, \end{aligned} \tag{10}$$

with the following appropriate boundary conditions:

$$\begin{aligned} &f(0) = 0, f'(0) = 1, \theta(0) = 1 - \delta_1, \varphi(0) \\ &\quad = 1 - \delta_2, f'(\infty) \longrightarrow 0, \theta(\infty) \longrightarrow 0, \varphi(\infty) \longrightarrow 0. \end{aligned} \tag{11}$$

The dimensionless numbers involved in equations (8) and (9) are

$$\begin{aligned} \gamma &= \left(\frac{\nu L}{U_0 R^2}\right)^{1/2}, K = \frac{\nu'}{\nu R^2}, \operatorname{Re} = \frac{U_0 R^2}{\nu}, \Pr \\ &= \frac{\mu c_p}{k}, \text{Sc} = \frac{\Pr \alpha_f}{D_B}, \delta_1 = \frac{c}{b}, \\ \text{Nb} &= \frac{\tau D_B(C_w - C_0)}{\nu}, \text{Nt} = \frac{\tau D_T(T_w - T_0)}{\nu T_\infty}, Gr \\ &= \frac{g\beta_T(T_w - T_0)x^3}{\nu^2}, \\ \text{Gr}^* &= \frac{g\beta_C(C_w - C_0)x^3}{\nu^2}\lambda_m = \frac{\text{Gr}}{\text{Re}_x{}^2}, N = \frac{\text{Gr}^*}{\text{Gr}}\gamma_E \\ &= \lambda_E\frac{U_0}{L}, \gamma_C = \lambda_C\frac{U_0}{L}. \end{aligned} \tag{12}$$

In respective order, the dimensionless parameters in equation (12) represent the curvature parameter, couple stress parameter, Reynolds number, Prandtl number, Schmidt number, thermal stratification parameter, solutal stratification parameter, Brownian diffusion parameter, thermophoresis parameter, Grashof number due to temperature, Grashof number due to concentration, mixed convection parameter, ratio of concentration to thermal buoyancy forces, relaxation time of heat, and mass flux.

The engineering physical quantities of interest in this study are the local skin friction coefficient, local Nusselt number, and local Sherwood number defined as follows:

$$C_f = \frac{2\tau_w}{\rho U_w^2}, \tau_w = \mu\left(\frac{\partial u}{\partial r}\right)_{r=R}, \mathrm{dRe}_x^{1/2} C_f = -f''(0), \mathrm{Nu}_x = \frac{-xq_w}{k(T_w - T_0)}, \mathrm{Sh}_x = \frac{-xj_w}{k(C_w - C_0)}, \tag{13}$$

with

$$q_w = -k\left(\frac{\partial T}{\partial r}\right)_{r=R}, j_w = -D_B\left(\frac{\partial C}{\partial r}\right)_{r=R}, \mathrm{Nu}_x \mathrm{Re}_x^{-1/2} = -\theta'(0), \mathrm{Sh}_x \mathrm{Re}_x^{-1/2} = -\phi'(0). \tag{14}$$

3. Numerical Solution

The Galerkin finite element method (GFEM) is the outstanding technique in solving engineering problems in particular fluid dynamics problems. GFEM is a variational method type in which shape functions are considered as exactly the same as the test function. In the weighted residual formulation of GFEM, we normally multiply the residual of the formulated DE by the weight function assumed to vanish in the Dirichlet boundary interval/region and set the integral over the whole domain equal to zero. We apply integral by parts to impose the Neumann and mixed/Robin-type boundary conditions (if they exist). The final step of the FEM is solving the assembled system of equations using the iterative type technique [17–20]. We reduce the higher order derivates involved in equations (8)–(10) with their boundary conditions (11) by substituting the function g as follows:

Assuming

$$f' = g. \tag{15}$$

The DE in (8)–(10) with the associated boundary conditions in (11) may be written in the form

$$(1+2\gamma\eta)g^{(2)} + 2\gamma g' - g^2 + fg' - K\,\mathrm{Re}\left(8\gamma^2 g^{(2)} + 8(1+2\gamma\eta)\gamma g^{(3)} + (1+2\gamma\eta)^2 g^{(4)}\right) + \lambda_m(\theta + N\varphi)\cos\alpha = 0, \tag{16}$$

$$(1+2\gamma\eta)\theta'' + 2\gamma\theta' + \mathrm{Pr\,Nb}(1+2\gamma\eta)\theta'\varphi' + \mathrm{Pr\,Nt}(1+2\gamma\eta)\theta'^2 - \mathrm{Pr}\left((\theta+\delta_1)g - f\theta'\right) - \mathrm{Pr}\,\gamma_E\left[f^2\theta'' - fg\theta' + g^2(\theta+\delta_1) - (\theta+\delta_1)fg'\right] = 0, \tag{17}$$

$$(1+2\gamma\eta)\left(\varphi'' + \frac{\mathrm{Nt}}{\mathrm{Nb}}\theta''\right) + 2\gamma\left(\varphi' + \frac{\mathrm{Nt}}{\mathrm{Nb}}\theta'\right) - \mathrm{Sc}\left((\varphi+\delta_2)g - f\varphi'\right) - \mathrm{Sc}\gamma_C\left[f^2\varphi'' - fg\varphi' + g^2(\varphi+\delta_2) - (\varphi+\delta_2)fg'\right] = 0, \tag{18}$$

with the following associated boundary conditions:

$$f(0) = 0, g(0) = 1, \theta(0) = 1 - \delta_1, \varphi(0) = 1 - \delta_2, g(\infty) \longrightarrow 0, \theta(\infty) \longrightarrow 0, \varphi(\infty) \longrightarrow 0. \tag{19}$$

We write the weighted integral forms of the boundary value problems in equations (15)–(18) over a predictable three-nodded linear element (η_e, η_{e+1}) as follows:

$$\int_{\eta_e}^{\eta_{e+1}} w_1\left\{f' - g\right\}d\eta = 0, \tag{20}$$

$$\int_{\eta_e}^{\eta_{e+1}} w_2\left\{(1+2\gamma\eta)g^{(2)} + 2\gamma g' - g^2 + fg' - K\,\mathrm{Re}\left(8\gamma^2 g^{(2)} + 8(1+2\gamma\eta)\gamma g^{(3)} + (1+2\gamma\eta)^2 g^{(4)}\right) + \lambda_m(\theta + N\varphi)\cos\alpha\right\}d\eta = 0, \tag{21}$$

$$\int_{\eta_e}^{\eta_{e+1}} w_3\left\{(1+2\gamma\eta)\theta'' + 2\gamma\theta' + \mathrm{Pr\,Nb}(1+2\gamma\eta)\theta'\varphi' + \mathrm{Pr\,Nt}(1+2\gamma\eta)\theta'^2 - \mathrm{Pr}\left((\theta+\delta_1)g - f\theta'\right) - \mathrm{Pr}\,\gamma_E\left[f^2\theta'' - fg\theta' + g^2(\theta+\delta_1) - (\theta+\delta_1)fg'\right]\right\} = 0, \tag{22}$$

$$\int_{\eta_e}^{\eta_{e+1}} w_4\left\{(1+2\gamma\eta)\left(\varphi'' + \frac{\mathrm{Nt}}{\mathrm{Nb}}\theta''\right) + 2\gamma\left(\varphi' + \frac{\mathrm{Nt}}{\mathrm{Nb}}\theta'\right) - \mathrm{Sc}\left((\varphi+\delta_2)g - f\varphi'\right) - \mathrm{Sc}\gamma_C\left[f^2\varphi'' - fg\varphi' + g^2(\varphi+\delta_2) - (\varphi+\delta_2)fg'\right]\right\}d\eta = 0, \tag{23}$$

with the following associated boundary conditions:

$$f(0) = 0, g(0) = 1, \theta(0) = 1 - \delta_1, \varphi(0) = 1 - \delta_2, g(\infty) \longrightarrow 0, \theta(\infty) \longrightarrow 0, \varphi(\infty) \longrightarrow 0, \tag{24}$$

where $w_1, w_2, w_3,$ and w_4 are weight functions and may be treated as the variation $f, g, \theta,$ and φ, respectively, and domain (η_e, η_{e+1}) denotes the interval of the boundary layer region.

In GFEM, the costmary practice of this step is searching for approximation solutions of the following form:

$$f = \sum_{j=1}^{3} f_j \psi_j, g = \sum_{j=1}^{3} g_j \psi_j, \theta = \sum_{j=1}^{3} \theta_j \psi_j, \varphi = \sum_{j=1}^{3} \varphi_j \psi_j, \quad (25)$$

with $w_1 = w_2 = w_3 = w_4 = \psi_i$ $(i = 1, 2, 3)$, the quadratic shape functions ψ_i are defined as

$$\begin{aligned}\psi_1^e &= \frac{(\eta_{e+1} - \eta)(\eta_{e+1} + \eta_e - 2\eta)}{(\eta_{e+1} - \eta_e)^2}, \psi_2^e \\ &= \frac{4(\eta - \eta_e)(\eta_{e+1} - \eta)}{(\eta_{e+1} - \eta_e)^2}, \psi_3^e \\ &= -\frac{(\eta - \eta_e)(\eta_{e+1} + \eta_e - 2\eta)}{(\eta_{e+1} - \eta_e)^2},\end{aligned} \quad (26)$$

where $\eta_e \le \eta \le \eta_{e+1}$.

Now we replace the approximate solution in equation (25) into equations (20)–(23), to obtain the finite element model for the equation which is given by

$$[K^e][Y^e] = [F^e], \quad (27)$$

where $[K^e]$ denotes the elemental stiffness matrix, $[Y^e]$ is the vector of elemental nodal variables (unknowns), and $[F^e]$ is the force vector expressed as follows:

$$\begin{aligned}[K^e] &= \begin{bmatrix} [K^{11}] & [K^{12}] & [K^{13}] & [K^{14}] \\ [K^{11}] & [K^{12}] & [K^{13}] & [K^{14}] \\ [K^{11}] & [K^{12}] & [K^{13}] & [K^{14}] \\ [K^{11}] & [K^{12}] & [K^{13}] & [K^{14}] \end{bmatrix}, [Y^e] \\ &= \begin{bmatrix} \{f\} \\ \{g\} \\ \{\theta\} \\ \{\phi\} \end{bmatrix}, [F^e] = \begin{bmatrix} \{h^1\} \\ \{h^2\} \\ \{h^3\} \\ \{h^4\} \end{bmatrix},\end{aligned} \quad (28)$$

where each $[K^{mn}]$ is of the order 3×3 and $[h^m]$ $(m, n = 1, 2, 3, 4)$ is of the order 3×1.

These matrices are defined as follows:

$$\begin{aligned}
K_{ij}^{11} &= \int_{\eta_e}^{\eta_{e+1}} \psi_i \frac{\partial \psi_j}{\partial \eta} d\eta, K_{ij}^{12} = -\int_{\eta_e}^{\eta_{e+1}} \psi_i \psi_j d\eta, K_{ij}^{13} \\
&= 0, K_{ij}^{14} = 0, K_{ij}^{21} = 0, \\
K_{ij}^{22} &= -(1 + 2\gamma\eta) \int_{\eta_e}^{\eta_{e+1}} \frac{\partial \psi_i}{\partial \eta} \frac{\partial \psi_j}{\partial \eta} d\eta + 2\gamma \int_{\eta_e}^{\eta_{e+1}} \psi_i \frac{\partial \psi_j}{\partial \eta} d\eta \\
&\quad + \int_{\eta_e}^{\eta_{e+1}} \psi_i \bar{f} \frac{\partial \psi_j}{\partial \eta} d\eta - \int_{\eta_e}^{\eta_{e+1}} \psi_i \bar{g} \psi_j d\eta \\
&\quad + 8K \operatorname{Re} \gamma^2 \int_{\eta_e}^{\eta_{e+1}} \frac{\partial \psi_i}{\partial \eta} \frac{\partial \psi_j}{\partial \eta} d\eta \\
&\quad + 8(1 + 2\gamma\eta)\gamma K \operatorname{Re} \int_{\eta_e}^{\eta_{e+1}} \frac{\partial \psi_i}{\partial \eta} \frac{\partial^2 \psi_j}{\partial \eta^2} d\eta \\
&\quad - K \operatorname{Re} (1 + 2\gamma\eta)^2 \int_{\eta_e}^{\eta_{e+1}} \frac{\partial^2 \psi_i}{\partial \eta^2} \frac{\partial^2 \psi_j}{\partial \eta^2} d\eta K_{ij}^{23} \\
&= \lambda_m \cos \alpha \int_{\eta_e}^{\eta_{e+1}} \psi_i \psi_j d\eta, K_{ij}^{24} \\
&= \lambda_m N \cos \alpha \int_{\eta_e}^{\eta_{e+1}} \psi_i \psi_j d\eta, K_{ij}^{31} = K_{ij}^{34} = 0, \\
K_{ij}^{32} &= -\Pr \delta_1 \int_{\eta_e}^{\eta_{e+1}} \psi_i \psi_j d\eta - \Pr \delta_1 \gamma_E \int_{\eta_e}^{\eta_{e+1}} \psi_i \bar{g} \psi_j d\eta \\
&\quad + \Pr \delta_1 \gamma_E \int_{\eta_e}^{\eta_{e+1}} \psi_i \bar{f} \frac{\partial \psi_j}{\partial \eta} d\eta, \\
K_{ij}^{33} &= -(1 + 2\gamma\eta) \int_{\eta_e}^{\eta_{e+1}} \frac{\partial \psi_i}{\partial \eta} \frac{\partial \psi_j}{\partial \eta} d\eta + 2\gamma \int_{\eta_e}^{\eta_{e+1}} \psi_i \frac{\partial \psi_j}{\partial \eta} d\eta \\
&\quad + \Pr \mathrm{Nb}(1 + 2\gamma\eta) \int_{\eta_e}^{\eta_{e+1}} \psi_i \overline{\varphi'} \frac{\partial \psi_j}{\partial \eta} d\eta \\
&\quad + \Pr \mathrm{Nt}(1 + 2\gamma\eta) \int_{\eta_e}^{\eta_{e+1}} \psi_i \overline{\theta'} \frac{\partial \psi_j}{\partial \eta} d\eta - \Pr \int_{\eta_e}^{\eta_{e+1}} \psi_i \bar{g} \psi_j d\eta \\
&\quad + \Pr \int_{\eta_e}^{\eta_{e+1}} \psi_i \bar{f} \frac{\partial \psi_j}{\partial \eta} d\eta - \Pr \gamma_E \int_{\eta_e}^{\eta_{e+1}} \psi_i \bar{f} \bar{f} \frac{\partial^2 \psi_j}{\partial \eta^2} d\eta \\
&\quad + \Pr \gamma_E \int_{\eta_e}^{\eta_{e+1}} \psi_i \bar{f} \bar{g} \frac{\partial \psi_j}{\partial \eta} d\eta - \Pr \gamma_E \int_{\eta_e}^{\eta_{e+1}} \psi_i \bar{g} \bar{g} \psi_j d\eta \\
&\quad + \Pr \gamma_E \delta_1 \int_{\eta_e}^{\eta_{e+1}} \psi_i \bar{f} \overline{g'} \psi_j d\eta, \\
K_{ij}^{42} &= -\mathrm{Sc}\delta_2 \int_{\eta_e}^{\eta_{e+1}} \psi_i \psi_j d\eta - \mathrm{Sc}\delta_2 \gamma_C \int_{\eta_e}^{\eta_{e+1}} \psi_i \bar{g} \psi_j d\eta \\
&\quad + \mathrm{Sc}\delta_2 \gamma_C \int_{\eta_e}^{\eta_{e+1}} \psi_i \bar{f} \frac{\partial \psi_j}{\partial \eta} d\eta, \\
K_{ij}^{43} &= -(1 + 2\gamma\eta) \frac{\mathrm{Nt}}{\mathrm{Nb}} \int_{\eta_e}^{\eta_{e+1}} \frac{\partial \psi_i}{\partial \eta} \frac{\partial \psi_j}{\partial \eta} d\eta \\
&\quad + 2\gamma \frac{\mathrm{Nt}}{\mathrm{Nb}} \int_{\eta_e}^{\eta_{e+1}} \psi_i \frac{\partial \psi_j}{\partial \eta} d\eta.
\end{aligned} \quad (29)$$

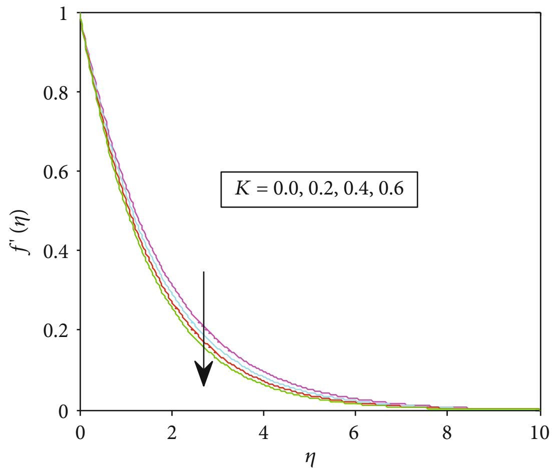

FIGURE 2: Velocity distribution for different values of the couple stress parameter.

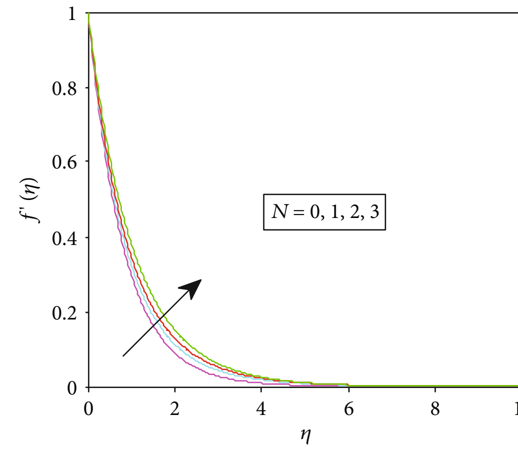

FIGURE 5: Velocity distribution for different values of N.

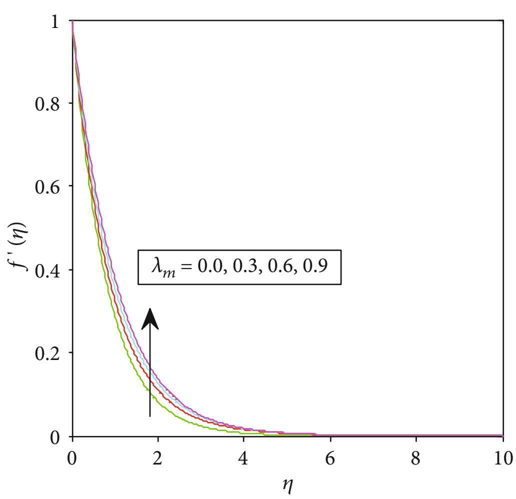

FIGURE 3: Velocity distribution for different values of the mixed convection parameter.

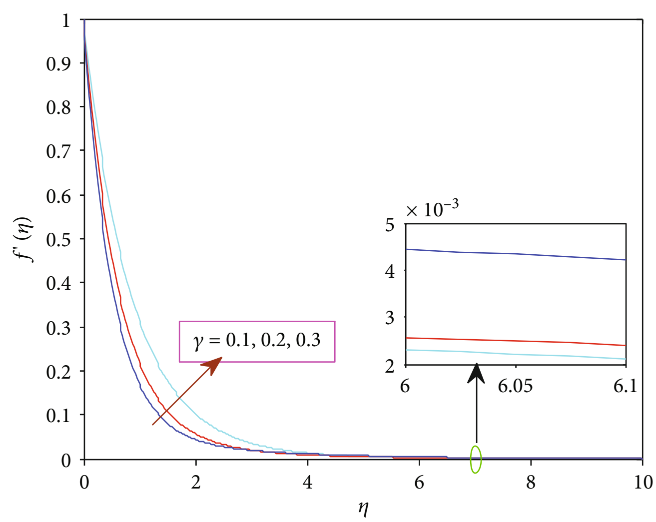

FIGURE 6: Velocity distribution for different values of the curvature parameter.

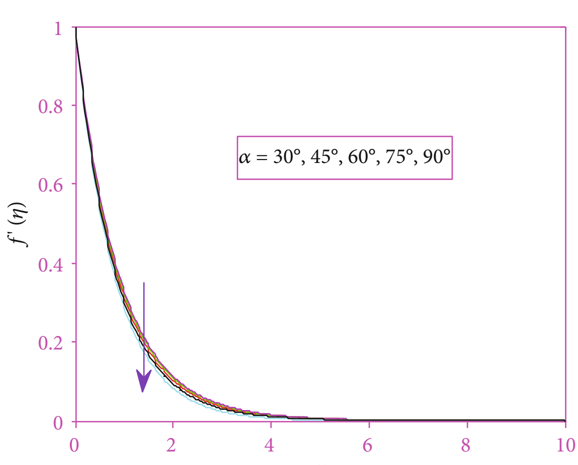

FIGURE 4: Velocity distribution for different inclinations.

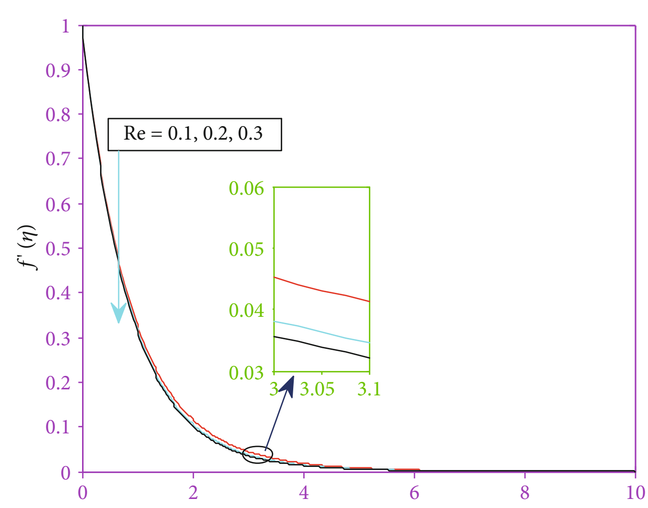

FIGURE 7: Velocity distribution for different values of the Reynolds number.

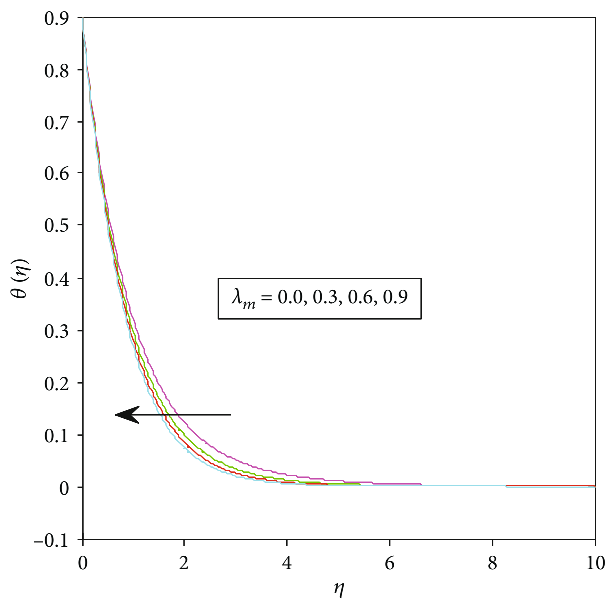

FIGURE 8: Temperature distribution for different values of the mixed convection parameter.

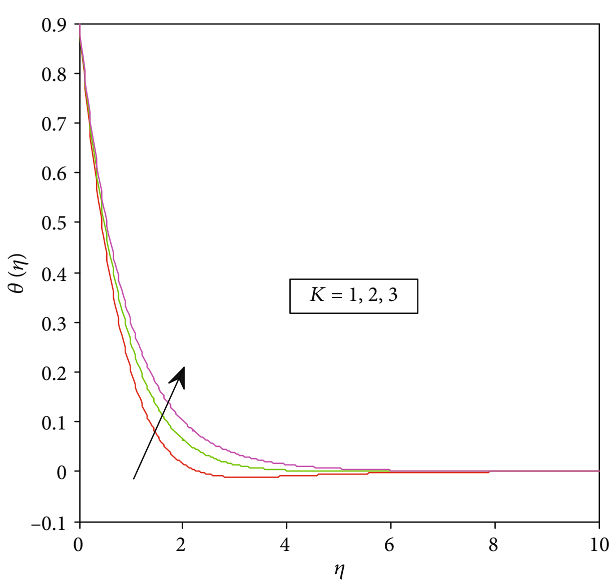

FIGURE 9: Temperature distribution for different values of the couple stress parameter.

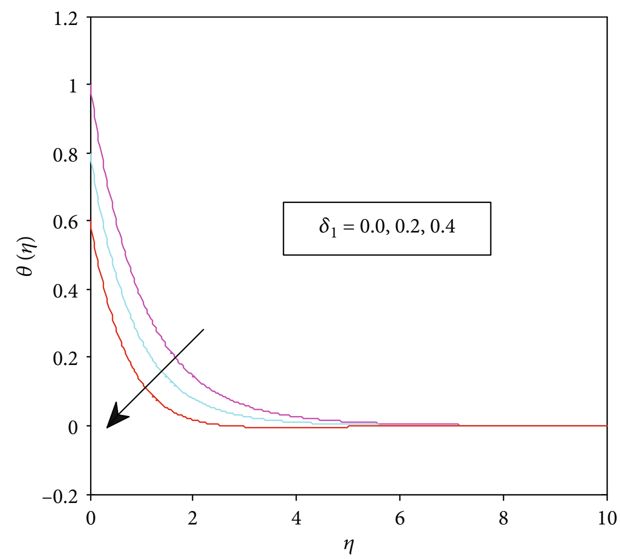

FIGURE 10: Temperature distribution for different values of the thermal stratification parameter.

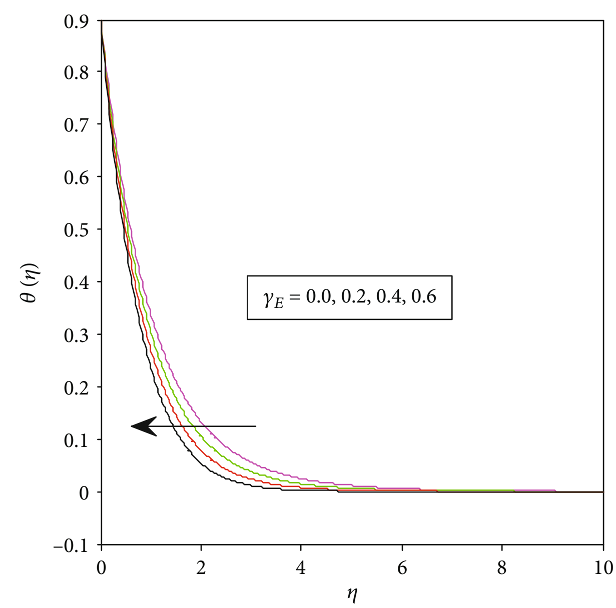

FIGURE 11: Temperature distribution for different values of the relaxation time of the heat flux.

4. Results and Discussion

The main aim of this scrutiny is to investigate the double stratified mixed convective flow of a couple stress nanofluid past an inclined stretching cylinder using the Cattaneo-Christov heat and mass flux model. The numerical solution for the proposed model is obtained using the Galerkin finite element method (GFEM). We performed a grid-invariance test or grid-convergence test to confirm the convergence of the series solution. The impacts of these relevant variables on velocity, temperature, concentration, local skin friction, heat transfer rate, and mass transfer rate are analyzed in both graphical and tabular forms. The default values of the present variables used to plot the graphs are chosen based on existing literature and parameter history and given as follows [18]:

$$\begin{aligned}\mathrm{Pr} &= 0.733, \lambda_m = 0, 2, \delta_1 = 0.1, K = 0.2, \gamma_E = 0.2, \gamma_C \\ &= 0.3, \mathrm{Sc} = 0.55, \delta_2 = 0.2, \mathrm{Re} = 0.3, N = 0.3, \alpha \\ &= 30^\circ, \gamma = 0.1, \mathrm{Nb} = 0.2, \mathrm{Nt} = 0.1.\end{aligned} \quad (30)$$

4.1. Velocity Field Analysis. Figures 2–7 are plotted to show the effects of the relevant parameters on velocity field in the boundary layer flow region. Figure 2 indicates that the velocity field is a decreasing function of a couple stress variable.

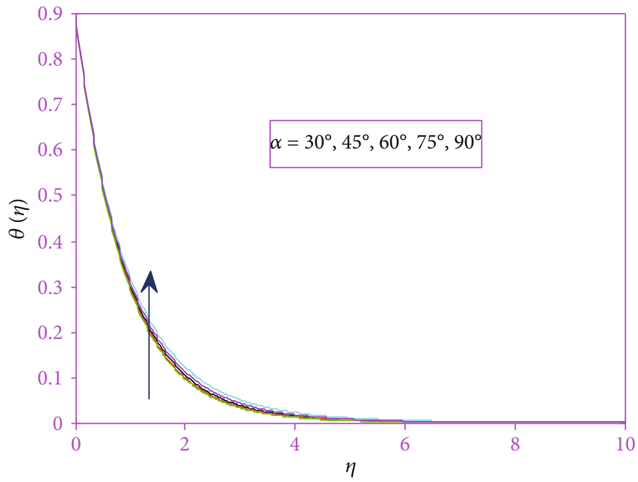

Figure 12: Temperature distribution for different inclinations.

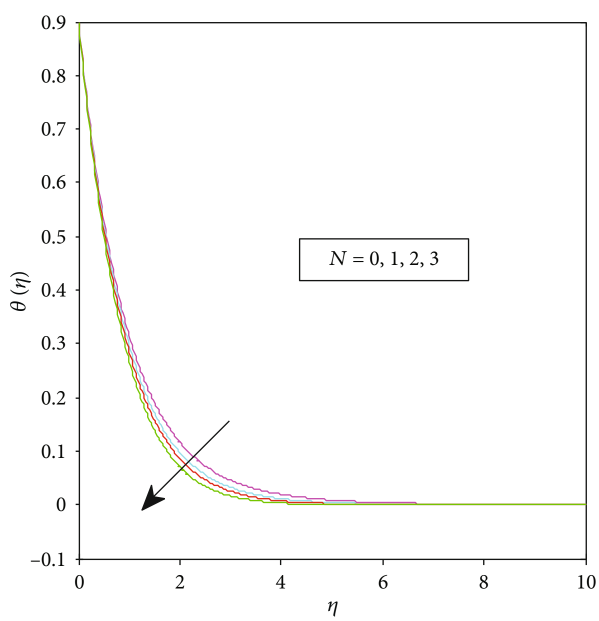

Figure 13: Temperature distribution for different values of N.

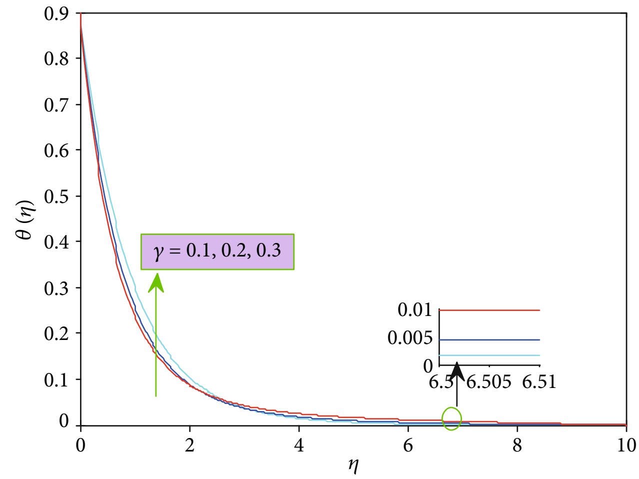

Figure 14: Temperature distribution for different values of the curvature parameter.

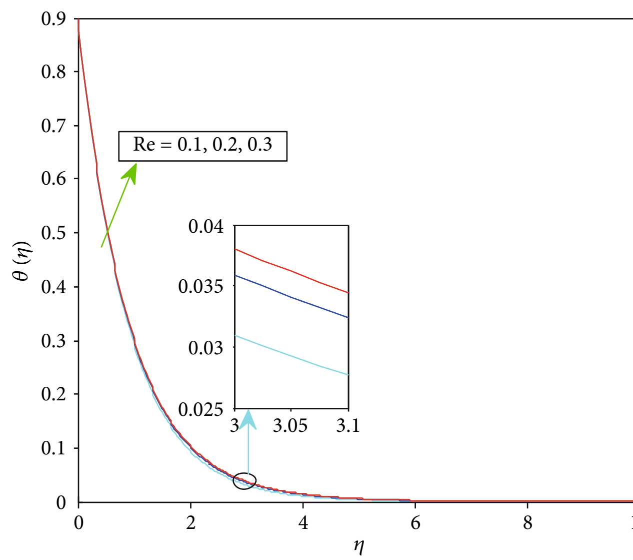

Figure 15: Temperature distribution for different values of the Reynolds number.

This is due to the fact that the increase in the couple stress parameter is responsible for the increase in the couple stress viscosity which acts as a slow downing agent that causes denser fluid. Quite opposite to the couple stress variable, the rise in the mixed convection parameter has the tendency to make faster the fluid movement. As mixed convection rises (cool the surface or heat the fluid), the buoyancy force will become stronger which dominates the viscous force (lower in viscosity) and this in turn translates the fluid flow from laminar to turbulence as revealed in Figure 3. According to Figure 4, relative to the x-axis when the angle of inclination α is maximized, the velocity starts declining because of the reduction in gravity. Figure 5 inspects that the velocity profile varies with different values of N. From the definition of N, it is crystal clear that the larger N is responsible for concentration dominance over thermal buoyancy force, which causes the increase in velocity of the fluid in the boundary layer regime. As pointed out in Figure 6, very close to the cylinder, the fluid movement is resisted with larger values of curvature, and far away from the cylinder, the velocity of the fluid is enhanced. Physically, higher curvature implies lower radius which in turn produces lower resistance of the fluid movement as revealed far away from the cylinder in Figure 6. Figure 7 depicts the effects of the Reynolds number on the velocity profile. Velocity distribution declined as the Reynolds number increases. This is due to the fact that, with a large Reynolds number, inertial force dominates over viscous force in the flow regime, and as a result, the velocity field decreases.

4.2. Temperature Distribution Analysis. Figures 8–16 are conspired to show the influences of the mixed convection parameter, couple stress parameter, thermal stratification

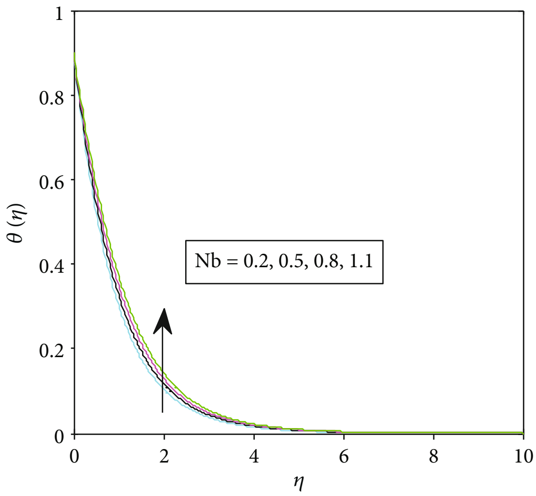

FIGURE 16: Temperature distribution for different values of Brownian diffusion.

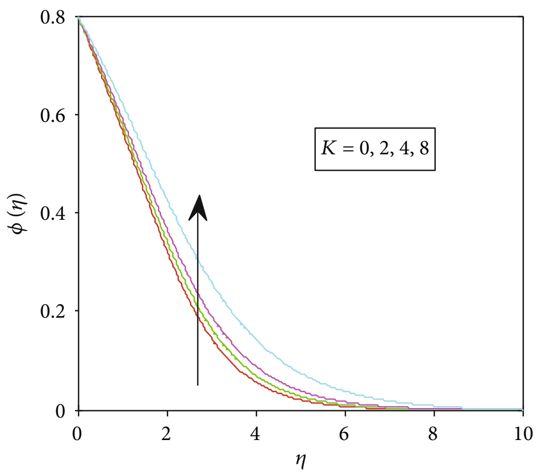

FIGURE 17: Concentration distribution for different values of the couple stress parameter.

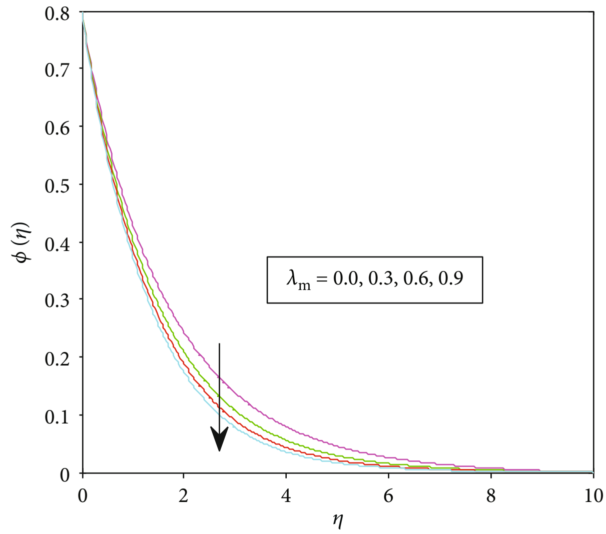

FIGURE 18: Concentration distribution for different values of the mixed convection parameter.

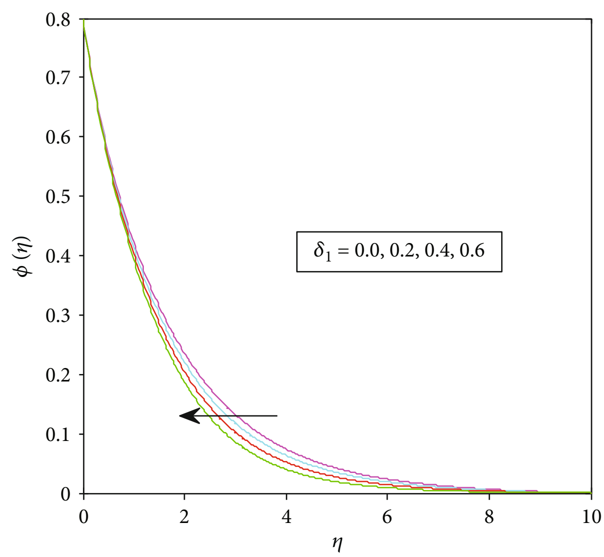

FIGURE 19: Concentration distribution for different values of the thermal stratification parameter.

parameter, relaxation time of heat flux, inclination, ratio of concentration to thermal buoyancy force, curvature, Reynolds number, and Brownian diffusion parameter on temperature distribution, respectively. Figure 8 is constructed to show the impacts of the mixed convection parameter on the temperature field. It is inspected that higher mixed convection in the fluid regime forced the cooling of the fluid, and quite the opposite condition is revealed with the rise of the couple stress parameter as indicated in Figure 9. The higher mixed convection is blamed for the larger thermal buoyancy force which results in a higher heat transfer rate and consequently decreases the temperature. The temperature profile is a decreasing function of the thermal stratification variable as plotted in Figure 10. Actually, the temperature variation between the surface and the ambient temperature eventually declines for larger values of the stratification parameter and decisively decreases the temperature distribution. The curve plotted in Figure 11 illustrates the temperature profile of the fluid with the thermal boundary layer thickness effectively decreasing for a longer relaxation time of the heat flux. In fact, the fluid with higher γ_E means that a longer time is mandatory for the fluid particle to transfer heat to its adjacent fluid particle, and this produces critical decline of the temperature in the flow regime. In Figure 12, it is observed that higher inclination of the cylinder enhances temperature in the boundary layer flow. Physically, higher inclination reduces the gravity which is the main cause for the decline of the heat transfer rate. This will maximize the temperature slightly. Figure 13 depicts the effects of N on temperature distribution. It is revealed that large values of N are responsible for the ultimate decline in temperature. This is not a surprising result as a larger N is responsible for the dominance of concentration over the thermal buoyancy force. As reported in Figure 14, the effect of the

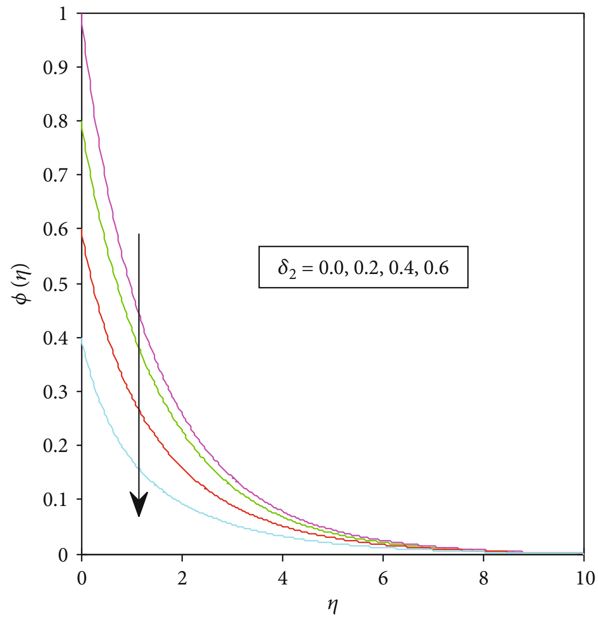

Figure 20: Concentration distribution for different values of the solutant stratification parameter.

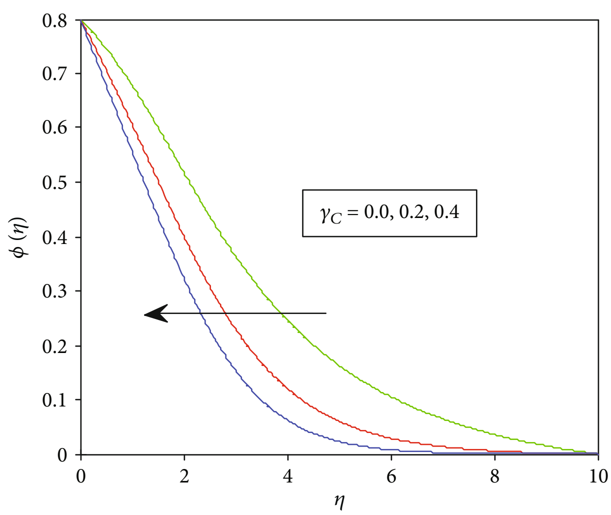

Figure 21: Concentration distribution for different values of the relaxation time of the mass flux.

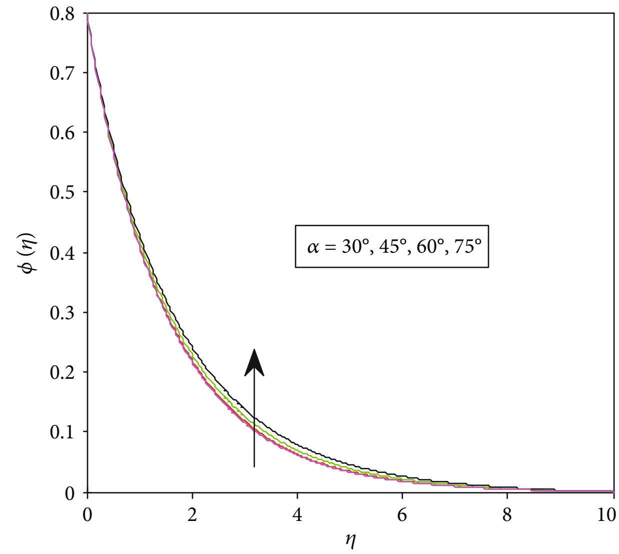

Figure 22: Concentration distribution for different inclinations.

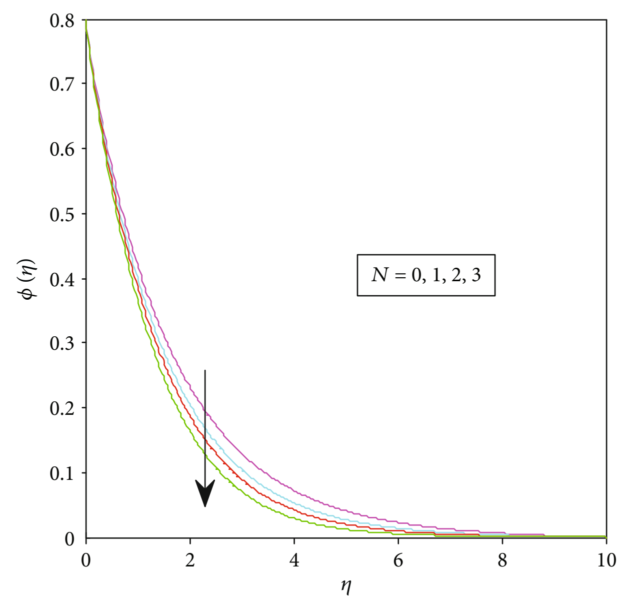

Figure 23: Concentration distribution for different values of N.

curvature on the temperature is not consistent throughout the analysis. Near the surface of the cylinder, the temperature has shown the tendency to decrease when the curvature increases. But the reverse phenomenon is observed away from the cylinder for lager values of η. In reality, a larger curvature is accountable for a larger thermal boundary layer thickness which consequently declines heat transfer rates due to the temperature rise at some distance from the cylinder as inspected in Figure 14. Figures 15 and 16 disclose that the temperature curve rises for both higher values of the Reynolds number and the Brownian diffusion parameter. The random movement of nanoparticles scattered in the base fluid is termed as Brownian motion. It may happen when nanoparticles collide with molecules of fluid (liquids or gases). Due to this movement of particles, the kinetic energy is enhanced, and ultimately, more heat is produced in the boundary layer regime. This is the cause for the fluid to be warmer (higher temperature).

4.3. Concentration Profile Analysis. Figures 17–28 are plotted to investigate the impacts of the couple stress parameter, mixed convection parameter, thermal stratification parameter, solutant stratification parameter, relaxation time of mass flux, inclination, ratio of concentration to thermal buoyancy forces, curvature parameter, Reynolds number, Schmidt number, Brownian diffusion parameter, and thermophoresis parameter on the concentration profile, respectively. As indicated in Figure 17, the concentration profile and concentration boundary layer thickness increase with

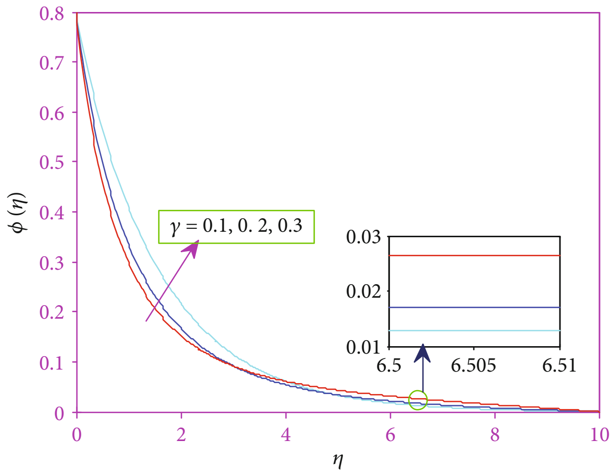

Figure 24: Concentration distribution for different values of the curvature parameter.

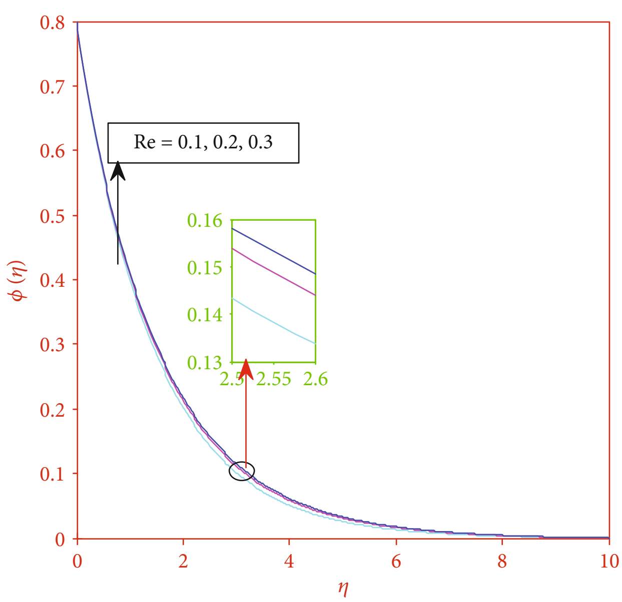

Figure 25: Concentration distribution for different values of the Reynolds number.

the enhancement of the couple stress parameter, and quite the opposite effect is revealed with the increasing values of the mixed convection parameter as shown in Figure 18. The concentration profile of the fluid is decreased significantly with larger positive values of thermal and solutant stratifications as inspected in Figures 19 and 20, respectively. As the solutant stratification increases, the convective potential between the surface of the cylinder and ambient fluid declines, and consequently, the concentration of the species of the fluid declines. Figure 21 shows the influence of the concentration relaxation parameter on concentration distribution. Both the concentration and its boundary layer thickness are decreasing functions of the concentration relaxation variable. The boosting of the inclination parameter has a positive impact on the concentration profile

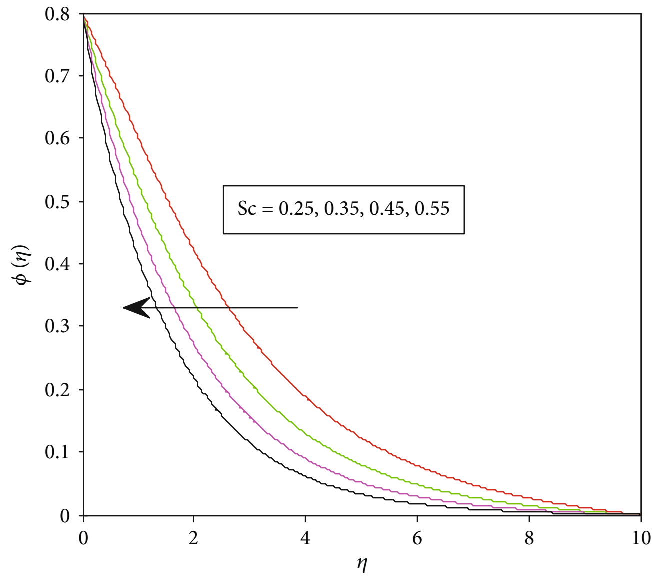

Figure 26: Concentration distribution for different values of the Schmidt number.

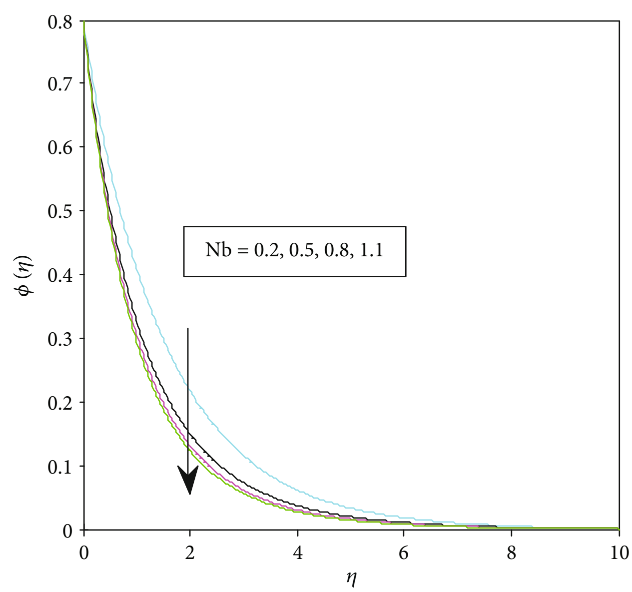

Figure 27: Concentration distribution for different values of Brownian diffusion.

curve as revealed in Figure 22. The higher inclination may force the gravity to reduce. Figure 23 elaborates the control of the ratio of the concentration to the thermal buoyancy force in the boundary layer flow region. The enhancement of this ratio is blamed for the dominance of the concentration buoyancy force over the thermal buoyancy force which may be responsible for the higher mass transfer rate in the flow regime. In this circumstance, the concentration of the species is strained to decline. The impact of curvature on concentration distribution is not consistent throughout the flow regime. Like velocity and temperature, near the surface of the cylinder, the concentration response is negative

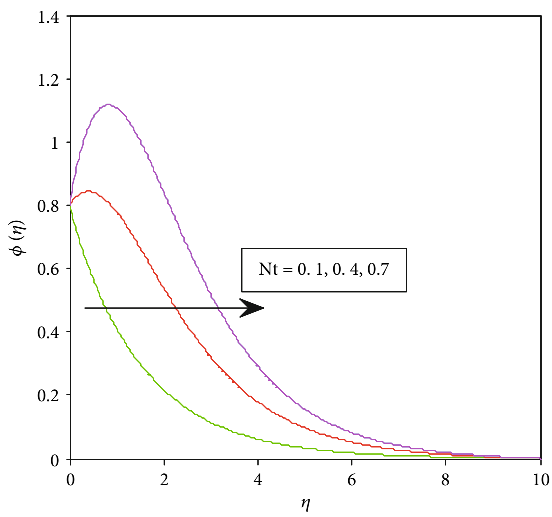

FIGURE 28: Concentration distribution for different values of the thermophoresis parameter.

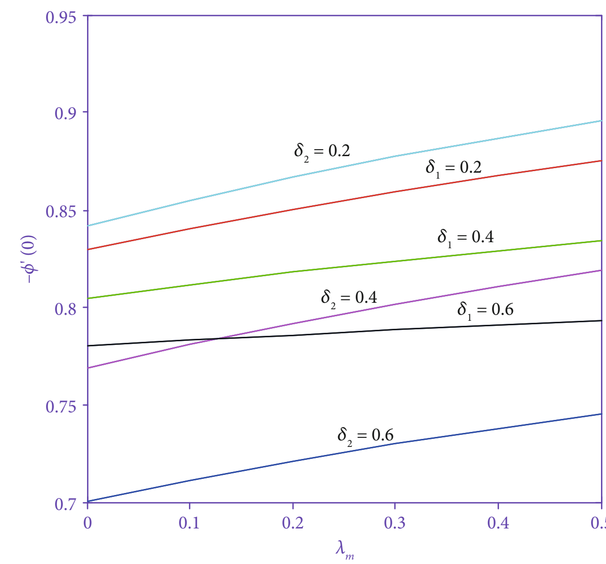

FIGURE 30: Effects of thermal and solutant stratification parameters on the mass transfer rate.

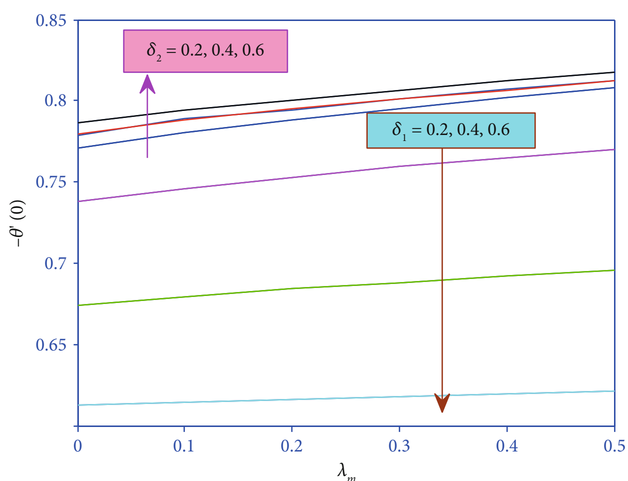

FIGURE 29: Effects of thermal and solutant stratification parameters on the heat transfer rate.

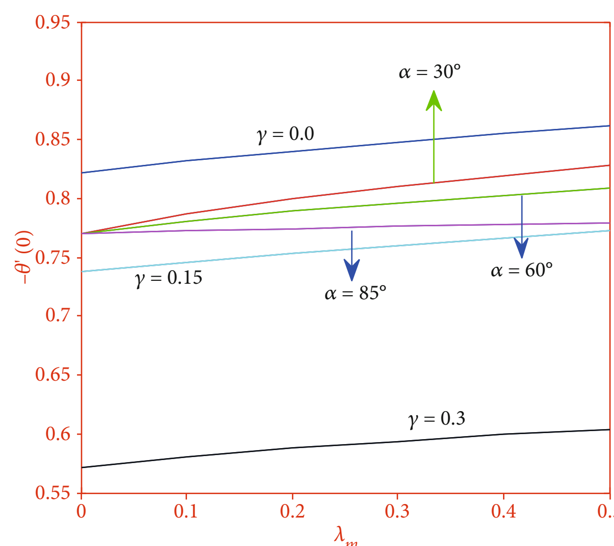

FIGURE 31: Effects of curvature and inclination parameters on the heat transfer rate.

(declined) as curvature advanced, while at some distance from the cylinder, the concentration response is positive (enhanced) as plotted in Figure 24. Moreover, the Reynolds number has a positive impact on the concentration of the species throughout this specific study as inspected in Figure 25. The concentration profile is reduced as the Schmidt number is increased (Figure 26). This is due to the fact that the Schmidt number and mass diffusivity are inversely related with each another. The concentration boundary layer thickness is also reduced with this scenario. The Brownian diffusion and the thermophoresis variables affected the concentration of the species differently as clarified in Figures 27 and 28. Increasing the values of the thermophoresis increases the concentration of the species in the stratified mixed convection couple stress nanofluid flow past the inclined cylinder while the reverse situation can be seen with the boosting values of the Brownian diffusion parameter.

Figures 29–33 anticipate the impacts of different governing parameters versus the mixed convection parameter on the local skin friction coefficient, local Nusselt number, and local Sherwood number. Figure 29 predicts the effects of thermal and solutant stratification parameters on the heat transfer rate of the fluid flow. The heat transfer rate in the flow decreases as thermal stratification increases, and the reverse impact is observed as the solutant parameter progress. In Figure 30, the effects of the thermal and solutant stratifications on the mass transfer rate are elaborated. When the two parameters advance, the response of the mass transfer rate is depreciation. Effects of curvature and inclination parameters on the heat transfer rate are illustrated in Figure 31. Both parameters have a decreasing impact on the

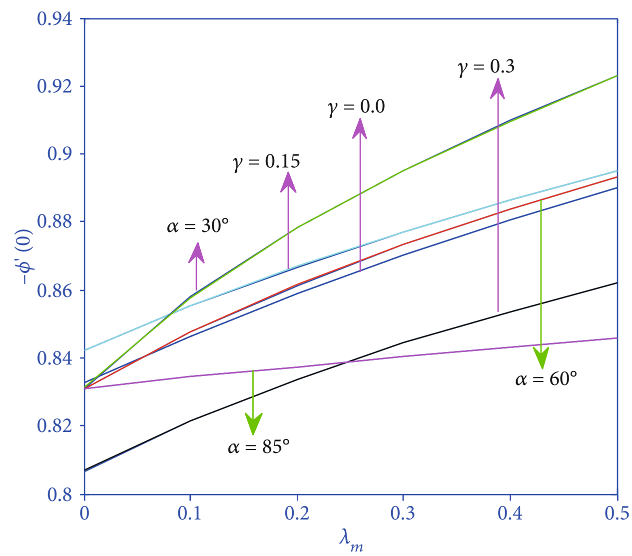

Figure 32: Effects of curvature and inclination parameters on the mass transfer rate.

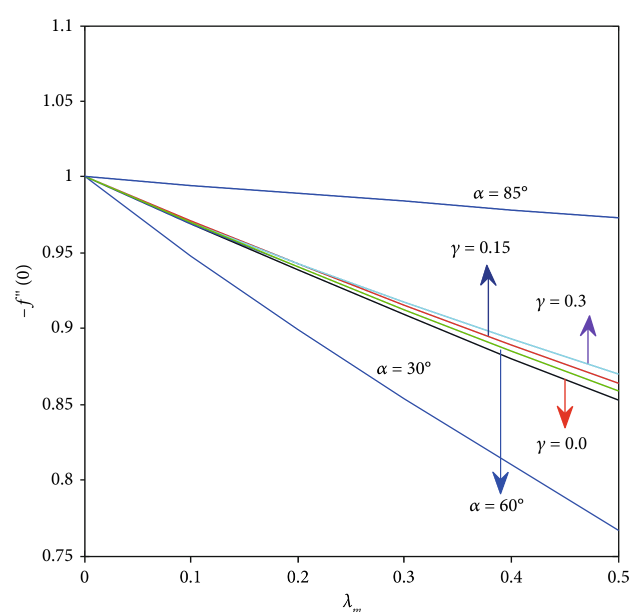

Figure 33: Effects of curvature and inclination parameters on the skin friction coefficient.

local Nusselt number in the flow regime. As predicted in Figure 32, curvature effects on the local Sherwood number is not consistent throughout the analysis. Very close to the cylinder and away from the cylinder, the variation in the heat transfer is quite opposite as the curvature enhances. Figure 33 shows that with larger inclination and curvature, the local skin friction coefficient enhances.

The grid-invariance test is performed to maintain the four-decimal-point accuracy. It is also called the grid-invariance test or grid-convergence test. We used this test to improve results using successively smaller step sizes for the calculations. We started by choosing a coarser mesh with

Table 1: Grid-independence test for velocity distributions $|f''(\eta)|$.

η	Coarse mesh with 100 elements ($h = 0.1$)	Medium mesh with 1000 elements ($h = 0.01$)	Fine mesh with 1500 elements ($h = 0.0067$)
1.5	1.01226	1.01224	1.01224
2.0	0.95250	0.95246	0.95247
2.5	0.92714	0.92709	0.92709
3.0	0.91507	0.91507	0.91500
3.5	0.90882	0.90873	0.90873
4.0	0.90537	0.90525	0.90525
4.5	0.90336	0.90321	0.90321
5.0	0.90215	0.90196	0.90196
5.5	0.90139	0.90117	0.90117
6.0	0.90092	0.90065	0.90065
6.5	0.90062	0.90030	0.90030
7.0	0.90043	0.90006	0.90006
7.5	0.90033	0.89989	0.89989
8.0	0.90027	0.89977	0.89977
8.5	0.90026	0.89969	0.89969
9.0	0.90027	0.89962	0.89963
9.5	0.90031	0.89958	0.89958

Table 2: Grid-independence test for temperature distributions $|\theta'(\eta)|$.

η	Coarse mesh with 100 elements ($h = 0.1$)	Medium mesh with 1000 elements ($h = 0.01$)	Fine mesh with 1500 elements ($h = 0.0067$)
1.5	0.85092	0.85096	0.85096
2.0	0.81487	0.81494	0.81495
2.5	0.80248	0.80266	0.80267
3.0	0.80255	0.79850	0.79851
3.5	0.79711	0.79730	0.79731
4.0	0.79697	0.79720	0.79721
4.5	0.79721	0.79721	0.79748
5.0	0.79755	0.79783	0.79784
5.5	0.79788	0.79818	0.79820
6.0	0.79817	0.79849	0.79851
6.5	0.79842	0.79875	0.79877
7.0	0.79861	0.79896	0.79898
7.5	0.79877	0.79912	0.79914
8.0	0.79890	0.79925	0.79927
8.5	0.79900	0.79936	0.79938
9.0	0.79908	0.79944	0.79946
9.5	0.79915	0.79950	0.79953

100 elements having a step size of $h = 0.1$. Then, increasing the number of elements ten times, we obtained a medium mesh with 1000 elements having a step size of $h = 0.01$. Finally, we have a fine mesh of 1500 elements with a step size of $h = 0.0067$ and get four-decimal-point accuracy in

Table 3: Grid-independence test for concentration distributions $|\phi'(\eta)|$.

η	Coarse mesh with 100 elements ($h = 0.1$)	Medium mesh with 1000 elements ($h = 0.01$)	Fine mesh with 1500 elements ($h = 0.0067$)
1.5	1.09566	1.09572	1.09572
2.0	0.99404	0.99414	0.99415
2.5	0.94507	0.94523	0.94523
3.0	0.91890	0.91911	0.91912
3.5	0.90389	0.90417	0.90418
4.0	0.89485	0.89485	0.89520
4.5	0.88918	0.88958	0.88960
5.0	0.88553	0.88598	0.88600
5.5	0.88311	0.88363	0.88365
6.0	0.88148	0.88205	0.88208
6.5	0.88037	0.88098	0.88101
7.0	0.87959	0.88025	0.88028
7.5	0.87904	0.87904	0.87977
8.0	0.87864	0.87938	0.87942
8.5	0.87835	0.87912	0.87916
9.0	0.87813	0.87894	0.87898
9.5	0.87796	0.87880	0.87885

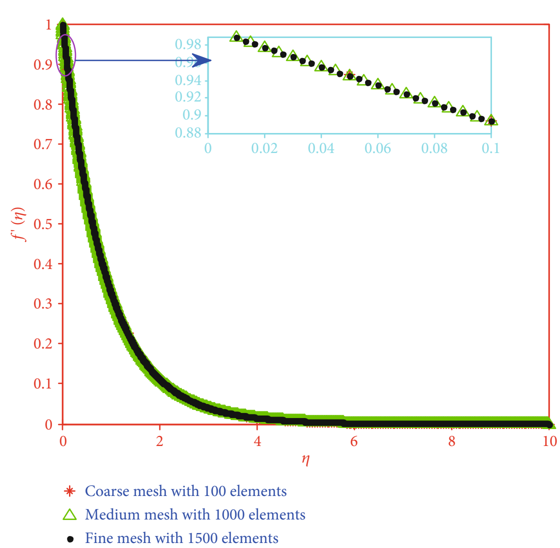

Figure 34: Grid-independence tests showing every fifth element of the mesh for velocity profile.

velocity, temperature, and concentration values. After increasing the number of elements more than 1500, the accuracy is not affected, but only to enlarge the compilation time. This is shown in Tables 1–3. Figures 34–36 are plotted to show the coarse, medium, and fine meshes for every fifth element of the mesh. Table 4 shows that our numerical technique is in good agreement with the existing literature. Table 5 is drawn to elaborate the effects of different governing parameters on the local skin friction coefficient, local Nusselt number, and local Sherwood number.

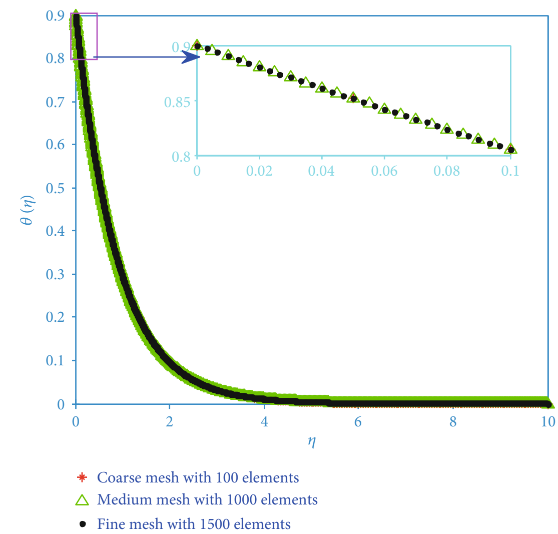

Figure 35: Grid-independence tests showing every fifth element of the mesh for temperature profile.

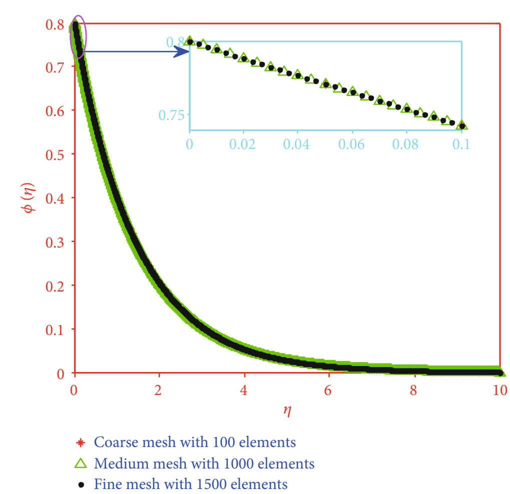

Figure 36: Grid-independence tests showing every fifth element of the mesh for concentration profile.

5. Conclusion

The Galerkin finite element method (GFEM) is applied to solve the problem of the double stratified mixed convective flow of the couple stress nanofluid over an inclined cylinder with the effects of a new heat and mass flux model. Then, the following remarks are made:

(i) Angle of inclination and material parameters have decreasing impact on velocity

(ii) Curvature impact on velocity, temperature, and concentration is not consistent throughout the analysis

(iii) Thermal stratification and inclination affected temperature in opposite ways

Table 4: Comparison of the values of the Nusselt number with Pr = Sc = 10.

Nt	$\lvert -\theta'(0) \rvert$											
	Nb = 0.1			Nb = 0.2			Nb = 0.3			Nb = 0.4		
	[21]	[20]	Present	[21]	[20]	Present	[21]	[20]	Present	[21]	[20]	Present
0.1	0.9524	0.95244	0.95238	0.5056	0.50561	0.50556	0.2522	0.25218	0.25218	0.1194	0.11940	0.11941
0.2	0.6932	0.69318	0.69318	0.3654	0.36536	0.36536	0.1816	0.18159	0.18159	0.0859	0.08588	0.08590
0.3	0.5201	0.52025	0.52018	0.2731	0.27313	0.27313	0.1355	0.13564	0.13554	0.0641	0.06424	0.06408
0.4	0.4026	0.40260	0.40260	0.2110	0.21100	0.21101	0.1046	0.10461	0.10460	0.0495	0.04962	0.04947
0.5	0.3211	0.32105	0.32108	0.1681	0.16811	0.16812	0.0833	0.08342	0.08330	0.0394	0.03932	0.03939

Table 5: Numerical values of local skin friction coefficient–$f''(0)$, local Nusselt number–$\theta'(0)$, and local Sherwood number–$\phi'(0)$.

Pr	λ_m	K	γ_E	γ_C	δ_1	δ_2	Nb	Sc	Nt	γ	α	N	$-f''(0)$	$-\theta'(0)$	$-\phi'(0)$
0.733	0.2	0.2	0.2	0.3	0.1	0.2	0.2	0.55	0.1	0.1	$\pi/6$	0.3	0.89955	0.79958	0.87875
1.00													0.90836	0.93873	0.88390
1.20													0.91311	1.02955	0.88808
0.733	0.3												0.85371	0.81032	0.89560
	0.4												0.80964	0.81984	0.91029
	0.2	0.0											0.88262	0.80757	0.89358
		0.1											0.89944	0.79962	0.87883
		0.2	0.3										0.90203	0.83372	0.88292
			0.4										0.90444	0.86792	0.88720
			0.2	0.4									0.90016	0.79782	0.90377
				0.5									0.90076	0.79607	0.92896
				0.3	0.3								0.92392	0.72763	0.84167
					0.5								0.94824	0.65602	0.80489
					0.1	0.4							0.90708	0.80452	0.80444
						0.6							0.91467	0.80936	0.73374
						0.2	0.1						0.89482	0.82989	1.04113
							0.3						0.90049	0.77238	0.82571
							0.2	0.15					0.88395	0.84092	0.45568
								0.35					0.89360	0.81604	0.68646
								0.55	0.2				0.89317	0.78620	1.03617
									0.3				0.88707	0.77278	1.19381
									0.1	0.2			0.90344	0.72218	0.87421
										0.3			0.89367	0.60254	0.83901
										0.1	$\pi/4$		0.91693	0.79522	0.87182
											$\pi/3$		0.94014	0.78908	0.86196
											$\pi/6$	0.2	0.90773	0.79703	0.87435
												0.1	0.91605	0.79434	0.86968

(iv) Solutant stratification, mixed convection, and relaxation time of the mass flux have decreasing effects on the concentration profile

(v) The concentration distribution of the flow is enhanced with the larger values of the Reynolds number and thermophoresis parameter whereas quite opposite effect is observed with higher values of the Schmidt number

Data Availability

The data included in this paper is available online without any restriction.

Conflicts of Interest

The authors declare that they have no conflicts of interest.

References

[1] A. Majeed, T. Javed, A. Ghaffari, and M. M. Rashidi, "Analysis of heat transfer due to stretching cylinder with partial slip and prescribed heat flux: a Chebyshev spectral Newton iterative scheme," *Alexandria Engineering Journal*, vol. 54, no. 4, pp. 1029–1036, 2015.

[2] T. Hayat, M. I. Khan, M. Waqas, and A. Alsaedi, "Newtonian heating effect in nanofluid flow by a permeable cylinder," *Results in Physics*, vol. 7, pp. 256–262, 2017.

[3] T. Hayat, S. Qayyum, A. Alsaedi, and S. Asghar, "Radiation effects on the mixed convection flow induced by an inclined stretching cylinder with non-uniform heat source/sink," *PLoS One*, vol. 12, no. 4, pp. 1–23, 2017.

[4] F. M. Abbasi, S. A. Shehzad, T. Hayat, and B. Ahmad, "Doubly stratified mixed convection flow of Maxwell nanofluid with heat generation/absorption," *Journal of Magnetism and Magnetic Materials*, vol. 404, pp. 159–165, 2016.

[5] K. U. Rehman, M. Y. Malik, T. Salahuddin, and M. Naseer, "Dual stratified mixed convection flow of Eyring-Powell fluid over an inclined stretching cylinder with heat generation/absorption effect," *AIP Advances*, vol. 6, no. 7, 2016.

[6] N. F. H. Mohd Sohut, A. S. Abd Aziz, and Z. M. Ali, "Double stratification effects on boundary layer over a stretching cylinder with chemical reaction and heat generation," *Journal of Physics: Conference Series*, vol. 890, no. 1, 2017.

[7] M. Ramzan, M. Bilal, and J. D. Chung, "Effects of thermal and solutal stratification on Jeffrey magneto-nanofluid along an inclined stretching cylinder with thermal radiation and heat generation/absorption," *International Journal of Mechanical Sciences*, vol. 131-132, pp. 317–324, 2017.

[8] K. U. Rehman, A. A. Khan, M. Y. Malik, and U. Ali, "Mutual effects of stratification and mixed convection on Williamson fluid flow under stagnation region towards an inclined cylindrical surface," *MethodsX*, vol. 4, pp. 429–444, 2017.

[9] K. U. Rehman, A. A. Malik, M. Y. Malik, N. Sandeep, and N. U. Saba, "Numerical study of double stratification in Casson fluid flow in the presence of mixed convection and chemical reaction," *Results in Physics*, vol. 7, pp. 2997–3006, 2017.

[10] A. Shafiq, I. Khan, G. Rasool, A. H. Seikh, and E. S. M. Sherif, "Significance of double stratification in stagnation point flow of third-grade fluid towards a radiative stretching cylinder," *Mathematics*, vol. 7, no. 11, pp. 1103–1117, 2019.

[11] M. Ijaz and M. Ayub, "Thermally stratified flow of Jeffrey fluid with homogeneous-heterogeneous reactions and non-Fourier heat flux model," *Heliyon*, vol. 5, no. 8, 2019.

[12] C. S. K. Raju, R. V. M. S. S. Kiran Kumar, S. V. K. Varma, A. G. Madaki, and P. Durga Prasad, "Transpiration effects on MHD flow over a stretched cylinder with Cattaneo–Christov heat flux with suction or injection," *Arabian Journal for Science and Engineering*, vol. 43, no. 5, pp. 2273–2280, 2018.

[13] W. Ibrahim and B. Hindebu, "Magnetohydrodynamic (MHD) boundary layer flow of Eyring-Powell nanofluid past stretching cylinder with Cattaneo-Christov heat flux model," *Nonlinear Engineering*, vol. 8, no. 1, pp. 303–317, 2019.

[14] K. Gangadhar, V. Ramana, D. Ramaiah, and B. R. Kumar, "Slip flow of a nanofluid over a stretching cylinder with Cattaneo-Christov flux model: using SRM," *International Journal of Engineering & Technology*, vol. 7, no. 4.10, 2018.

[15] K. A. Kumar, V. Sugunamma, N. Sandeep, and J. V. R. Reddy, "MHD stagnation point flow of Williamson and Casson fluids past an extended cylinder: a new heat flux model," *SN Applied Sciences*, vol. 1, no. 7, 2019.

[16] S. Asad, A. Alsaedi, and T. Hayat, "Flow of couple stress fluid with variable thermal conductivity," *Applied Mathematics and Mechanics*, vol. 37, no. 3, pp. 315–324, 2016.

[17] D. Gupta, L. Kumar, O. A. Beg, and B. Singh, "Finite-element analysis of transient heat and mass transfer in microstructural boundary layer flow from a porous stretching sheet," *Computational Thermal Sciences*, vol. 6, no. 2, pp. 155–169, 2014.

[18] W. Ibrahim and G. Gadisa, "Finite element analysis of couple stress micropolar nanofluid flow by non-Fourier's law heat flux model past stretching surface," *Heat Transfer Research*, vol. 48, no. 8, pp. 3763–3789, 2019.

[19] D. Gupta, L. Kumar, and B. Singh, "Finite element solution of unsteady mixed convection flow of micropolar fluid over a porous shrinking sheet," *The Scientific World Journal*, vol. 2014, Article ID 362351, 11 pages, 2014.

[20] M. Goyal and R. Bhargava, "Finite element solution of double-diffusive boundary layer flow of viscoelastic nanofluids over a stretching sheet," *Computational Mathematics and Mathematical Physics*, vol. 54, no. 5, pp. 848–863, 2014.

[21] W. A. Khan and I. Pop, "Boundary-layer flow of a nanofluid past a stretching sheet," *International Journal of Heat and Mass Transfer*, vol. 53, no. 11–12, pp. 2477–2483, 2010.